이학석사 학위논문

Opposition Effect of Asteroid (25143) Itokawa

소행성 (25143) 이토카와의 충 효과

2017년 8월

서울대학교 대학원

물리천문학부 천문학전공

이 민 경

Abstract

On a planetary surface, the reflected brightness is not uniformly risen near zero phase angle (i.e. the angle between Sun − object − observer, $\alpha \approx 0°$), which is known as 'opposition effect'. Because most of outer Solar System objects (e.g. asteroids and Kuiper-Belt Objects) have been observed near the zero phase angles, it is of importance to understand the physical mechanism for the opposition effect. However, little is known about the cause of the opposition mechanism, although two possible hypotheses, that is, a shadow hiding effect and a coherent backscattering effect have been suggested mostly based on the theoretical studies (e.g. Hapke 1986, 2002).

In 2005, Japanese sample returning interplanetary mission, Hayabusa, succeeded in obtaining regolith sample from S-type asteroid (25143) Itokawa. It is expected that the data may provide a clue for the better understanding of the opposition mechanism on the asteroidal surface, because some of the images were intentionally acquired near the opposition. We analyzed images were taken with the Asteroid Multi-band Imaging Camera (AMICA) at b (429 nm), v (553 nm), w (700 nm), and p (960 nm)-bands, and derived the slope of the reflectance (hereafter, S_{OE}) around the zero phase angles.

As a result, we found that (1) S_{OE} changes drastically at $\alpha<1.2°$-$1.5°$, whereas becomes constant at $\alpha>1.2°$-$1.5°$, (2) this trend does not show wavelength dependence for all four bands, (3) incidence and emission angles do not make a significant influence on S_{OE}. From these results, we conjectured that the coherent backscattering effect dominates on Itokawa under phase angle of 1.2°-1.5° while the shadow hiding effect stands out over the phase angle.

Note that the evidence of coherent backscattering effect is hardly confirmed on any Solar System objects because 'the shadow of the observer' itself obscures the

signal near the opposition ($\alpha<1.4°$), making it impossible to recognize the effect. Accordingly, we would insist that the telescopic imaging capability from a distant place (9 km from the surface) as well as the multiband data of AMICA enable to obtain definitive evidence for the mechanisms of the opposition effect.

Keyword: asteroid − asteroids: (25143) Itokawa − asteroids: surface properties

Student Number: 2014-22384

Table of Contents

List of Figures

List of Tables

Chapter 1. Introduction

1.1. What is the Opposition Effect?

A study of the planetary surface provides the information such as particles covered regolith of the planetary object, to understand its physical properties and formation. One of the useful tools to study the planetary surface is opposition effect, which is the sharply enhanced surge of the intensity of the reflected light on a planetary surface, when the phase angle (i.e. Sun − object − observer's angle) is nearly zero degree. It was noticed for the first time on the ring of Saturn (Seeliger, as cited in Hapke 2012a). Later the effect was observed on the S-type asteroid (20) Massalia, providing the first usage of the term "Opposition Effect". Opposition effect has been confirmed on various types of minor objects. For example, Hapke (1990) analyzed opposition effect for outer satellites such as Jovian satellites, and Hapke et al. (1993) measured this effect for Lunar surface using Apollo samples. Deau et al. (2009) investigated satellites of our planets and Saturn's rings to study about the environment of these objects. Likewise, Kuiper Belt objects (KBOs, Belskaya et al. 2003; Schaefer et al. 2009) and Centaurs (Schaefer et al. 2009) were observed at near opposition. This effect confirmed on the asteroid surfaces in diverse types, such as S-type (Dovgopol et al. 1992; Gehrels 1956; Gehrels & Taylor 1977), E-type (Harris et al. 1989), and V-type (Hasegawa et al. 2014).

Opposition effect provides the information about the microscopic structure of granular medium with its mechanisms, which is not greatly related to the composition. The ideas of the shadow hiding effect and coherent backscattering effect remain a matter of debates about the cause of opposition effect for several decades. The former, shadow hiding opposition effect (SHOE) means the opposition effect from the absence of shadow cast by a particle. To be specific, the medium that

consists of sparse and large particles compared with the wavelength casts a shadow on individual particles or makes a particulate tunnel at large phase angle (Hapke 2012a). However, this shadow gradually disappears as phase angle approach to zero degrees. SHOE depends on the microstructure of the medium such as particle the particle size distribution, and porosity, for instance, in the extremely packed regolith, the medium does not have SHOE (Hapke 2012a). This effect can be seen through single scattering because the extinction shadow could be illuminated in multiple scattering; therefore, it usually works on the dark surface. In contrast, coherent-backscattering opposition effect (CBOE) arises from constructive interference of wavelets when the light rays scattered by more than two particles. If the incident rays which scatter the opposite direction but same path inside more than one particle interfere each other at zero phase angle, the brightness becomes enhanced about four times of the individual intensity (Hapke 2012a). The CBOE is affected by the mean photon free path; thus, longer wavelength and low opacity could make CBOE in the narrow angle. This effect acts on the multiple scattering that it usually observed with a small width in high albedo surfaces such as E-type asteroid or icy satellite like Europa (e.g. Helfenstein et al. 1998; Spjuth et al. 2012). However, it could occur in a large complex particle as well (Hapke 2002; Shkuratov & Helfenstein 2001).

In the early stage of the study for opposition effect, researchers in this research field have debated the primary mechanism of the effect. For example, in the case of lunar opposition effect, Hapke et al. (1993) asserted CBOE as the principal mechanism of opposition effect on the lunar surface, while Buratti et al. (1996) insisted the dominance of SHOE by analyzing Clementine data. However, Helfenstein et al. (1997) suggested that the lunar opposition effect could be explained by the combination of CBOE and SHOE using their theoretical model. For asteroids, Belskaya and Shevchenko (2000) found the relation of physical quantities of various asteroids such as albedo and color of the asteroids that both SHOE and CBOE

dominate on the moderate albedo surfaces. In the case of satellites, Helfenstein et al. (1998) found both mechanisms on Europa's surface.

Opposition effect has been observed frequently on the surfaces of various objects in the Solar System via ground-based observations or space telescope such as Hubble Space Telescope (e.g. Verbiscer et al. 2005). For remote sensing observation, Hayabusa, which is Japanese asteroid sample returning mission, succeeded in bringing the sample on a S-type asteroid, (25143) Itokawa (hereafter, Itokawa). During the mission period, especially on 13 October 2005, the spacecraft intentionally seize an opportunity to obtain Itokawa image at opposition. The appearance of Itokawa near the opposition is represented in Figure 1. The later missions such as Rosetta by ESA also succeeded in observing opposition effect of E-type asteroid like (2867) Steins (Spjuth et al. 2012), and M-type asteroid such as (21) Lutetia (Hasselmann et al. 2016).

1.2. The Purpose of This Study

From several observational types of researches which are mentioned the previous section, opposition effect could be discriminated by its angular width—SHOE has wide angular width than that of CBOE—in phase curve (i.e. a curve of the relationship between the phase angle and the reflectance or radiance factor). However, CBOE and SHOE are hard to separate each other in the phase curve, if SHOE occurs at small phase angle (Hapke 2012a). Moreover, the regional variation of this effect using disk-resolved analysis has not been studied well so far.

The key to solving the above difficulty is to know the type of scattering (i.e. single scattering or multiple scattering). The albedo of a planetary surface has been derived from reflectance: the albedo increases with increasing the reflectance. Moreover, high albedo surface is dominated by the multiple scattering, while low

albedo surface is dominated by the single scattering. From these factors, the reflectance would be an essential information to conjecture the mechanism of opposition effect. The geometric albedo of Itokawa was derived as 0.19 (Lederer et al. 2008), but the value of the radiance factor (the ratio of the reflectance of the observed surface to the reflectance of the perfect diffusive surface) increases up to 0.3 from around 2.0 at 553nm (v-band). This value is predominantly larger than those of other asteroids including mission target bodies. It means Itokawa is a good object to investigate the relation and the regional variation of opposition effect with disk-resolving analysis, which has not been studied well so far.

In summary, the purpose of this research is to characterize the mechanism of the opposition effect on Itokawa utilizing its opposition effect images taken with one of the instruments of Hayabusa spacecraft, the asteroid multiband imaging camera (AMICA). We introduce the physical properties of Itokawa and the data acquisition using AMICA in following chapter (Chapter 2). The result of the profiles of the opposition effect and its visualizations is exhibited in Chapter 3. Finally, the interpretation of the opposition effect on Itokawa's surface is discussed in the final chapter, Chapter 4.

Chapter 2. Observation and Image Analysis

2.1 Observations of Itokawa Near the Opposition

Figure 1 - Figure 2 shows the images of Itokawa, in which the bottom images were taken near the zero-phase angle (i.e., the opposition) and the top images were obtained at the phase angle of 10° (top) for comparison. We organized of image groups on the basis of the rotational phases and as “SET”. We got two sets, SET1 and SET2, and total eight images are included in each set. These eight images can be categorized following AMICA multi-bands. Only four bands in AMICA filters b (429nm), v (553nm), w (700nm), and p (960nm), are used for this study due to the number of corresponded images. All images for this study is four binning image so that the resolution is 81.96″/pixel—the original pixel resolution of AMICA is 20.49″/pixel. To sum up, two images taken at slightly different phase angle but in the same band consist of a pair, and total four bundles are involved in SET1 or SET2. Table 1 describes the image file in each set that used for this study.

The bottom panels in Figure 1 and Figure 2 exhibit the representative images of each set. Two Itokawa images were taken at different rotation phase on the Western side of Itokawa. (Figure 3 in Demura et al. 2006). In these figures, one of the distinct features of the opposition effect is that small topographical structures such as boulders and craters are hard to be resolved in the images near the opposition. The other feature is that the brightness of the rim on Itokawa disk is enhanced like the radiance at the center of the disk, so the images look flatly without undulations. Another remarkable point is the biggest boulder of Itokawa which is called as Yoshinodai (the red dashed circle in the bottom panel of Figure 2, and a protrusion on the left side the disk in Figure 1). Yoshinodai boulder is hidden in the rest part at

the opposition, so that its brightness cannot be discriminated from the surroundings.

Figure 3 − 4 illustrates the calculated phase angles at each point in the images and the radiance factor (*I/F*, the ratio of the reflectance on the observed surface to the reflectance on the perfectly diffused surface such as Lambertian surface), for the SET1 (Figure 3) and SET2 (Figure 4). The exact opposition, in other words, the location of the Sun is positioned by an arrow symbol in Figure 3 and Figure 4. These figures show the representative images (taken in v-band) of a pair in each set that the left column has smaller phase angle, otherwise is larger phase angle. According to Figure 3 − Figure 4, the phase angle of SET1 is lower than that of SET2, and *I/F* is also brighter than that of SET2. Although the whole disk looks almost uniform in Figure 1 and Figure 2, *I/F* variation still exists in both figures.

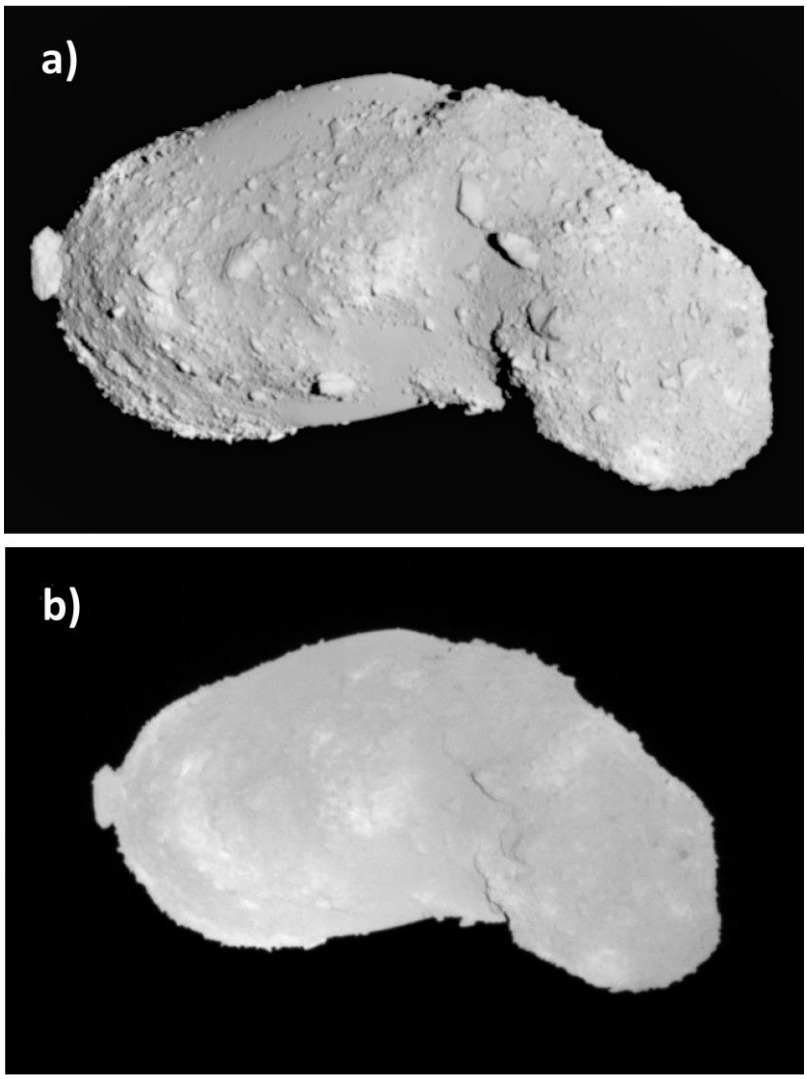

Figure 1 a) The obtained images of Itokawa taken at the phase angle $\boldsymbol{\alpha} \approx \mathbf{10}°$. b) The image (non−binning image) for SET 1 (see the body) for this study taken around opposition ($\boldsymbol{\alpha} = \mathbf{0.05}° - \mathbf{2.3}°$, See Figure 3c).

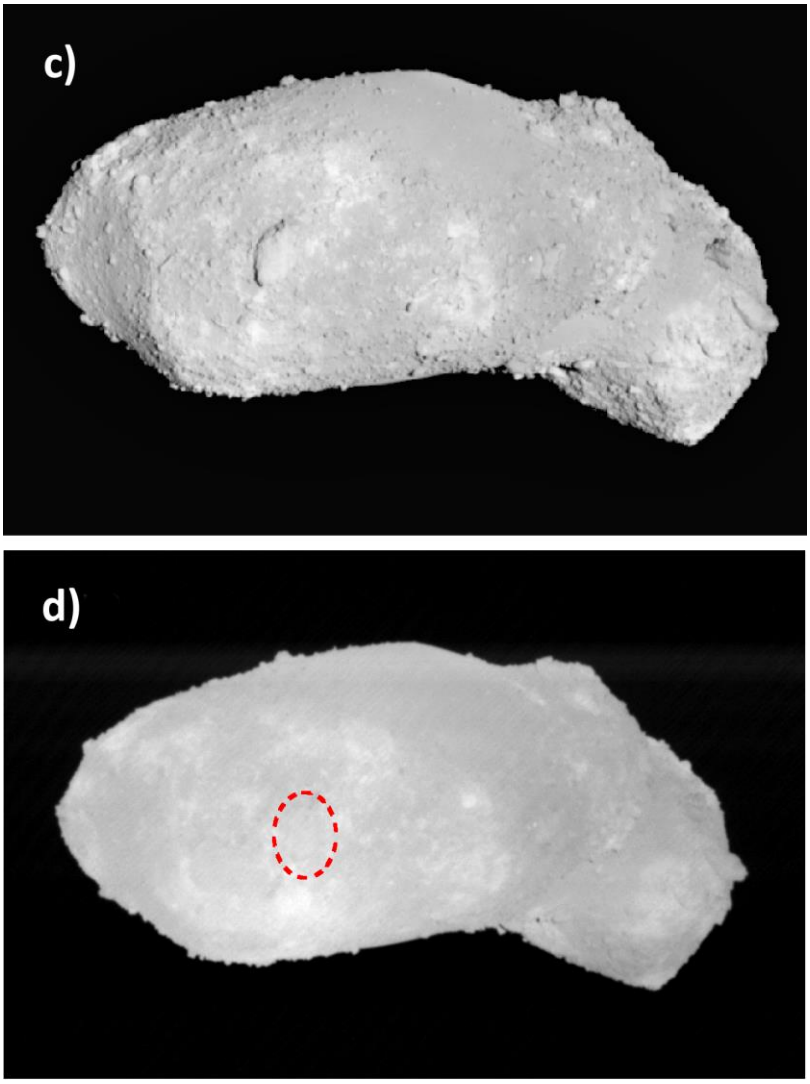

Figure 2 Continued. c) The obtained image taken around $\alpha \approx 10°$. d) The non−binning image for SET 2 for this study taken at opposition ($\alpha = 0.24° - 2.5°$). A red dashed circle indicates the location of Yoshinodai, which is the biggest boulder on Itokawa.

Table 1 The information of AMICA images used for this study.[①]

Set	Fine name	Filter (Wavelength)	Phase angle coverage [degree]
SET1	ST_2455782773_b.fits	b (429nm)	0.06 – 2.22
	ST_2457157533_b.fits		0.76 – 2.3
	ST_2455786613_v.fits	v (553nm)	0.06 – 2.21
	ST_2457161422_v.fits		0.76 – 2.3
	ST_2455790502_w.fits	w (700nm)	0.06 – 2.2
	ST_2457165278_w.fits		0.77 – 2.31
	ST_2455794390_p.fits	p (960nm)	0.06 – 2.2
	ST_2457469150_p.fits		0.77 – 2.3
SET2	ST_2456105349_b.fits	b (429nm)	0.26 – 2.07
	ST_2457506969_b.fits		1.07 – 2.52
	ST_2456109221_v.fits	v (553nm)	0.26 – 2.06
	ST_2457510874_v.fits		1.07 – 2.52
	ST_2456113110_w.fits	w (700nm)	0.25 – 2.05
	ST_2457514731_w.fits		1.07 – 2.52
	ST_2457169150_p.fits	P (960nm)	0.24 – 2.04
	ST_2457518587_p.fits		1.06 – 2.52

① All of AMICA raw images are disclosed on "Hayabusa Project Science Data Archive (http://darts.isas.jaxa.jp/planet/project/hayabusa/)".

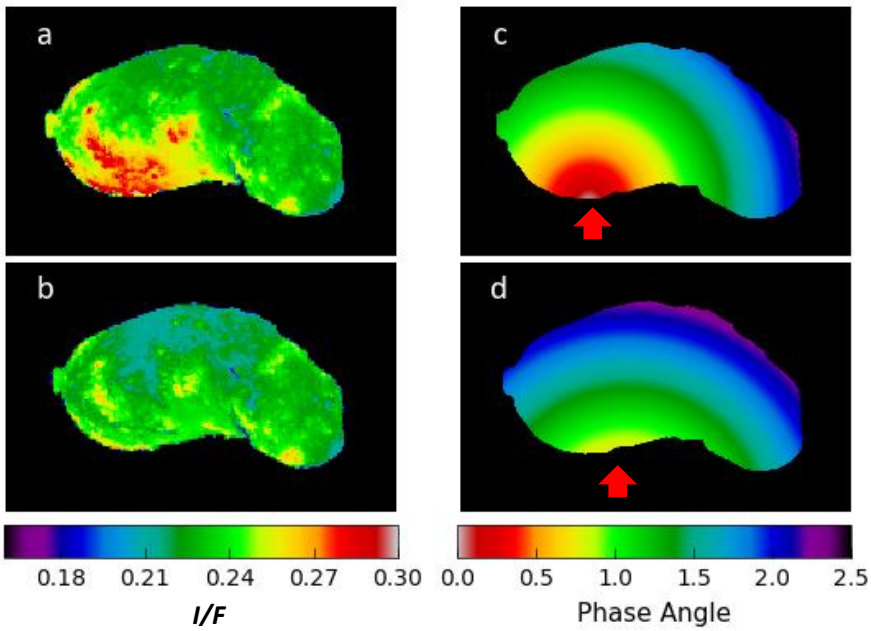

Figure 3 The false color v-band image for SET1. a) *I/F* values near the opposition, b) *I/F* values at the relatively large phase angle, c) phase angles near the opposition, d) phase angles at the relatively large phase angle. The red arrows point the exact opposition.

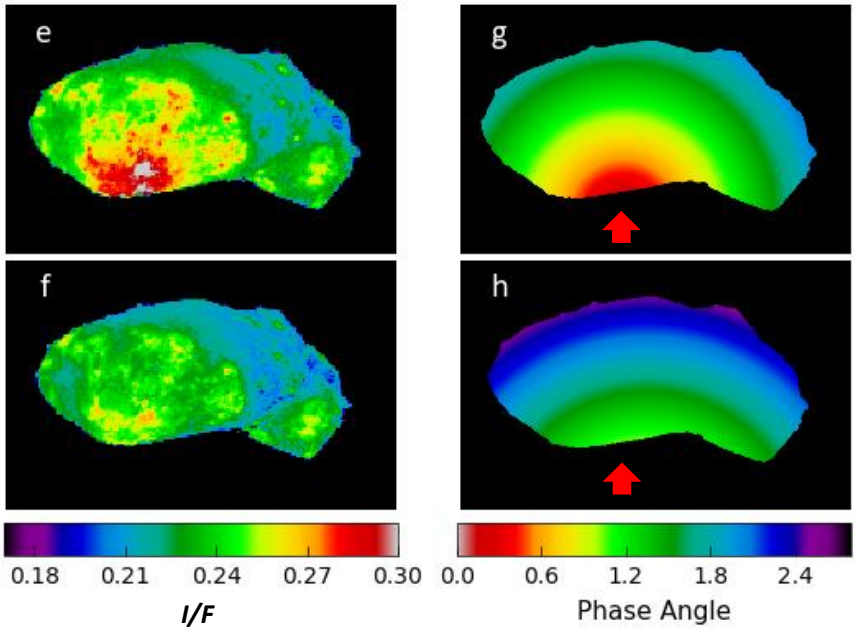

Figure 4 The similar illustration to Figure 3, but for SET2. a) *I/F* profile (near opposition). b) *I/F* profile at relatively large phase angle. c) Phase angle profile (near opposition). d) Phase angle profile at the relatively large phase angle. The exact opposition is indicated by red arrows.

2.2 Data Reduction for Hayabusa/AMICA Images

Remote-sensing observation follows similar data reduction process of ground-based observation. However, AMICA is a frame-transfer CCD camera without a mechanical shutter. The detector's part consists of the image area and the frame storage area (Ishiguro et al. 2010). In our data analysis, initially, streak lines (readout-smear) that occur during frame transfer were removed onboard by using zero exposure images. However, some of AMICA images are needed to subtract the readout-smear manually, because in the early of October 2005, Hayabusa lost its reaction wheel, which brings mismatch between exposure image and smear image (see, Ishiguro et al. 2010). Ishiguro et al. (2010) established the image processing method for AMICA. Ishiguro (2014) further described a technique to subtract a halo of AMICA images which is generated by scattered light inside the instrument. We strictly followed all processing steps in Ishiguro et al. (2010) and Ishiguro (2014) to analyze opposition effect with AMICA data. All processed images are converted into the radiance factor using the v-band image.

Ishiguro et al. (2010) suggested the calibration factor of each AMICA multi-bands—ul (381nm), b (429nm), v (553nm), w (700nm), x (861nm), p (960nm) and zs (1008nm)—to match the spectra of Itokawa to ground-based observation (Binzel et al. 2001; Lowry et al. 2005). However, it did not consider the scattering light correction. We updated this calibration factor with the internal halo correction, following the same manner in Ishiguro et al. (2010). These values are multiplied with the image of the radiance factor which is divided by the image in v-band. Table 2 shows the updated calibration factors for b, v, w and p bands, respectively. Figure 3 − Figure 4 are the images after all of the pre-processing.

Table 2 Updated the scale factor for this study. Original factors without the scattered correction described in Ishiguro et al. (2010).

Filter (wavelength)	Updated scale factor (error)
b (429 nm)	1.252 (0.003)
v (553 nm)	1.000 (-)
w (700 nm)	0.660 (0.004)
p (960 nm)	2.416 (0.016)

2.3 Characterization of the Opposition Effect

The most previous studies about opposition effect have conducted using a theoretical model. Hapke model (Hapke 1981, 1984, 1986, 2002, 2008, 2012b) is one of the models for photometric analysis, which has been widely utilized in planetary studies (e.g. Lederer et al. 2008; Spjuth et al. 2012; Ishiguro et al. 2014; Hasselmann et al. 2016). Although the Hapke model is precisely fitted to observed data and contains a lot of physical information including opposition effect, we do not employ the model because a large number of parameters make hard to get a unique solution. Moreover, at near opposition most physical quantities except parameters related with opposition effect may be insignificant (e.g. surface roughness). We focus on opposition effect of asteroid Itokawa in the narrow range of phase angle and its regional variation with the relation between the reflectance and opposition effect. For these reasons, we employed a simple model with a single parameter, S_{OE}, instead of using existing models.

The parameter, S_{OE} characterizes the opposition slope: how strongly opposition effect occurs. It is defined by the linear slope formula which is widely known. As we exhibited in Section 2.1 (Figure 1 and Figure 2), the surface of Itokawa shows nearly uniform brightness, and there is no conspicuous roughness. It means other properties such as the surface roughness may be ignorable for our study. Moreover, the degree of opposition effect could be regarded as the slope of the non-linear curve because of its definition, the non-linear spike of intensity. Therefore, the opposition behavior can be simplified to the linear approximation by taking a few phase angle intervals (not exceed 0.8°). The slope parameter, S_{OE}, can be defined as following equation:

$$\mathbf{S_{OE,i}} = \frac{\left(\frac{I}{F}\right)_{2,i} - \left(\frac{I}{F}\right)_{1,i}}{\alpha_{2,i} - \alpha_{1,i}} \qquad (1)$$

where i is a pixel index located on Itokawa disk in an image, and subscripted numbers (i.e. 1 and 2) mean the image in each image set. The first number in the subscript "2" corresponds the image at larger phase angle while "1" is the image at smaller phase angle.

The two pixels which are applied to equation (1) should be placed at the same position in real geography. As we described in Section 2.1, the images that are used for this study make up a pair (image 1 and image 2) for each band, which is an element of SET1 or SET2. We selected two pixels from a certain location. These pixels have subscript i. *I/F* and the phase angle information of the pixels are applied to equation (1), and the equation (1) returns S_{OE}. However, because the asteroid rotates continuously, the selected AMICA images were not taken at exactly the same rotational phase. Therefore, the guide to confirm whether each selected pixel in each image of the bundle has the same location in real is needed. The shape model of Itokawa is one of the solutions to this problem. The next section (Section 2.4) described the method how shape model could be utilized in this study.

2.4 Geometric Information

Raw observed images do not contain the geometric information such as incidence angle (i), emission angle (e), angle and phase angle (α). The accurate geometric information is significant for opposition effect study, because this effect has a strong correlation with the phase angle near the opposition. For remote-sensing observation, these geometry angles (i.e. incidence, emission, and phase angle) could be obtained

by an ancillary tool in particular SPICE, which is developed by NASA NAIF (Navigation and Ancillary Information Facility) team. SPICE provides the auxiliary data (e.g. position of a planetary object) collected from spacecraft operation as “kernels”.

Note that Itokawa has highly irregular shape unlike planets and major satellites, Thus, it could not be regarded as a simple solid figure such as a sphere or an ellipsoid. In the case of our study, both shape model and the ancillary data are needed for proper geometry. For this reason, we accessed the geometric information for each pixel of AMICA images by utilizing “Plate Renderer.” Dr. Naru Hirata at the University of Aizu in Japan has developed Plate Renderer, and it simulates a view of AMICA at given observation time by combining the information from the shape model of Itokawa and NASA SPICE kernels. This tool provides the simulated AMICA images and additional images which contain geometrical information at given time with ".fits" format. The followings are the outputs of Plate Renderer:

1. Incidence angle and emission angle [degree]
2. Phase angle [degree]
3. Distance between each plate of the shape model and the spacecraft [km]
4. Strike azimuth [degree]
5. Latitude and longitude [degree]
6. The modeled reflectance on surface with Hapke model

We slightly modified this tool to get the plate ID of shape model of Itokawa. The plate ID is used in identifying the exact location to match two pixels in image 1 and image 2. There is a problem that the pixel size of AMICA image is much bigger than a facet of the shape model of Itokawa. Thanks to the modification, however, we obtained the most of the pixels on Itokawa disk.

2.5 Data Restriction with Criteria

We could not utilize all data from Itokawa disk due to a mismatch of the rotational phase. As we mentioned above, AMICA could not catch the images at exact one Itokawa rotation intervals because of the finite exposure time. This mismatch could bring high uncertainty to our analysis. Especially, the uncertainty is large in the images of SET1, which has the smallest phase angle. Thus, we should set three criteria to exclude some of the data points in high uncertainty. The three criteria are as followings:

1. We limited the difference of the phase angle ($\Delta\alpha$) which is greater than 0.3°. Because, the slope parameter is defined as the ratio of the difference of *I/F* and that of phase angle. It means the uncertainty increases as $\Delta\alpha$ decrease. Thus, we need to determine the lower limit of the difference between α_1 and α_2, i.e., $\Delta\alpha$.
2. We exclude the rim of Itokawa's disk for all images that we used for this study. The rotational appearances of Itokawa in an image pair do not match exactly due to asteroid rotation during exposure. Plate Renderer helps us to extract pixels at the topographically same location. The most of the discrepancies are concentrated on the edge of the asteroid disk. Therefore, we eliminated the uncertainty by excluding the edge.
3. In the case of incidence and emission angle dependency, we considered two cases: (1) $i < 90°$ and (2) $i < 60°$. This condition only used for the investigation whether the geometric angle is valid to the opposition effect or not.

Chapter 3. Result

3.1 The Maps of the Slope Parameter

Figure 5 shows the maps of slope parameter for each band in SET1 and SET2. These maps were prepared following equation (1). Each column corresponds the image of four AMICA band in each set that has the same rotational appearance. The exact opposition is indicated by red arrows, which are located near the darkly-colored portions on the images. The color means the value of the slope parameter, S_{OE}. It has a negative sign so that the radiance factor increases as phase angle decreases. In other words, the high negative value coincides with the strong opposition effect. Hereafter, we regard the value of the slope parameter as its absolute value to prevent confusing, for instance, “high value” means “highly negative number”.

Comparing the Figure 5 and Figure 3 − Figure 4, S_{OE} steadily follows the phase angle distribution. It is important to notice that the strong opposition effect (dark color) exhibits only narrow region near the opposition. This means that the S_{OE} rapidly changes centering on the opposition point, but this variation on S_{OE} becomes small (thus, almost uniform) at larger phase angle (outside the border of blue and red color). Careful investigation of these maps allows us to notice that both SET1 and SET2 show the highest S_{OE} in w-band that has the brightest spectra in AMICA bands, but some portion of p-band in SET1 represents slightly stronger opposition than w-band. The whitish regions on the right side of each panel show the case of $\alpha_1 > \alpha_2$ due to rotation of Itokawa, which should be ignored in this research. These components are ignored for our analysis, because of the criterion, $\Delta\alpha \leq 0.3$ (the criterion 1 in Section 2.5).

In Figure 5 we could not found a remarkable regional variation. The distribution

of high S_{OE} (bluer color) is similar to phase angle distribution in Figure 3 and Figure 4, rather than *I/F* distribution in the same figures. Moreover, we could not find outstanding regional variation over bluer part (orange and yellow colors) in Figure 5. However, we discovered that Yoshinodai is still invisible on the map for SET2 (the right column in Figure 5).

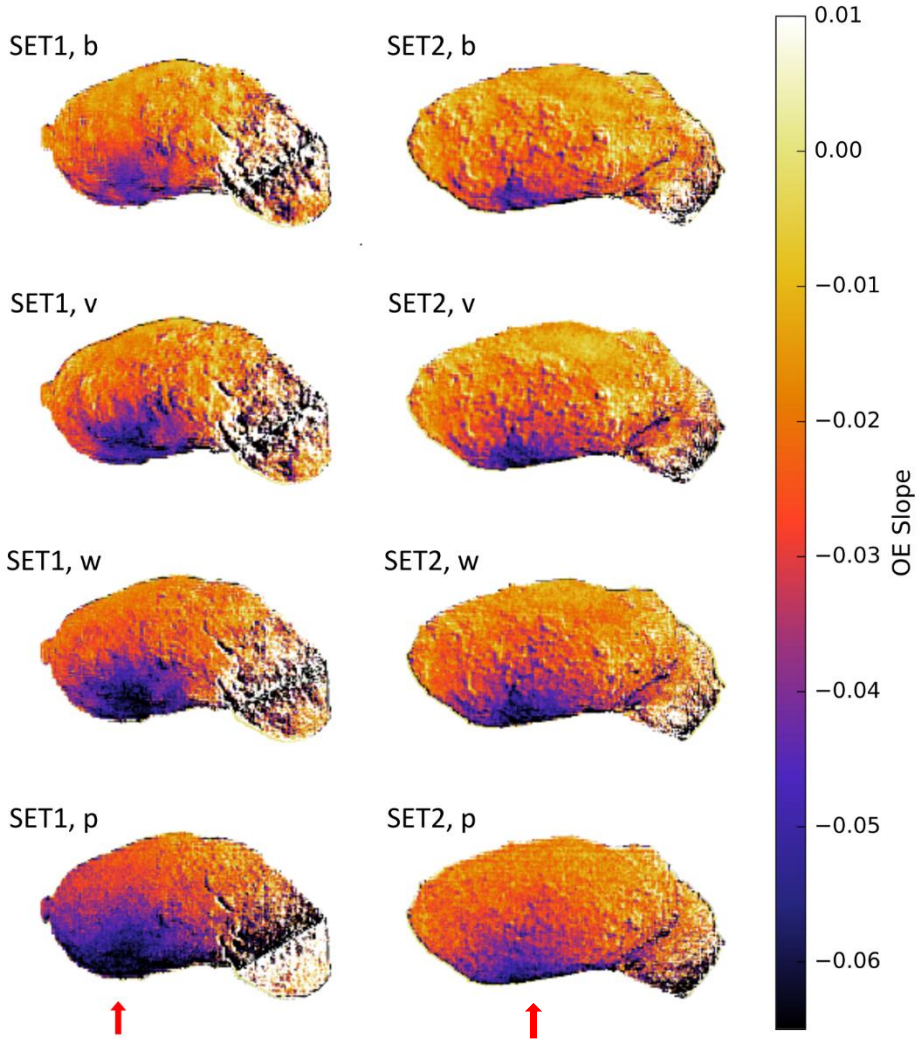

Figure 5 The map of slope parameter ($\mathbf{S_{OE}}$) in both SET1 and SET2. The opposition effect is stronger as the color on the map is darker. Red arrows show the position of exact opposition. The right side of each sub−panel could be ignored due to the limit of data. See Section 2.5.

3.2 Phase Angle Dependency of the Opposition Effect on Itokawa

S_{OE} is illustrated with phase angle in Figure 6 − Figure 9. The horizontal axis denotes the average value in phase angles between two selected pixels (i.e. $(\alpha_{2,i} + \alpha_{1,i})/2$, where i is the index of the pixel), while the vertical axis corresponds to S_{OE} calculated from equation (1). All data was binned with the phase angle of 0.2° to reduce the random noise of the images. We plotted the average S_{OE} within the bins by black hollow symbols (circle, square, diamond and triangle), and original data by gray dots. The standard error, which is known as the standard deviation divided by the number of data points in each bin, is too small to be seen in the figures. We plotted phase angle − S_{OE} relation for each AMICA band in each set among four figures. Figure 6 and Figure 8 shows the phase angle dependency of S_{OE} for each band in SET1 and SET2 that incidence and emission angles are less than 90°. Figure 7 and Figure 9 coincide to the same relation to Figure 6 and Figure 8, but the angle of incidence and emission are restricted within 60°. However, comparing these plots, we noticed that the appearance of curves does not have a notable difference.

We found a specific trend in Figure 6 − Figure 9 even though original data is still highly scattered after applying criteria. In visual inspection, there is an inflection point that the trend of phase angle − *I/F* relation turns around the mean phase angle from 1.2° to 1.5°, comparing original data (gray dots). The wavelength is longer in the order of counter-clockwise for the subpanels in Figure6 − Figure 9. However, there is no significant difference in the trend, even though all p-band result shows almost a linearly diagonal line. In other words, the wavelength dependency of the inflection point does not show clearly.

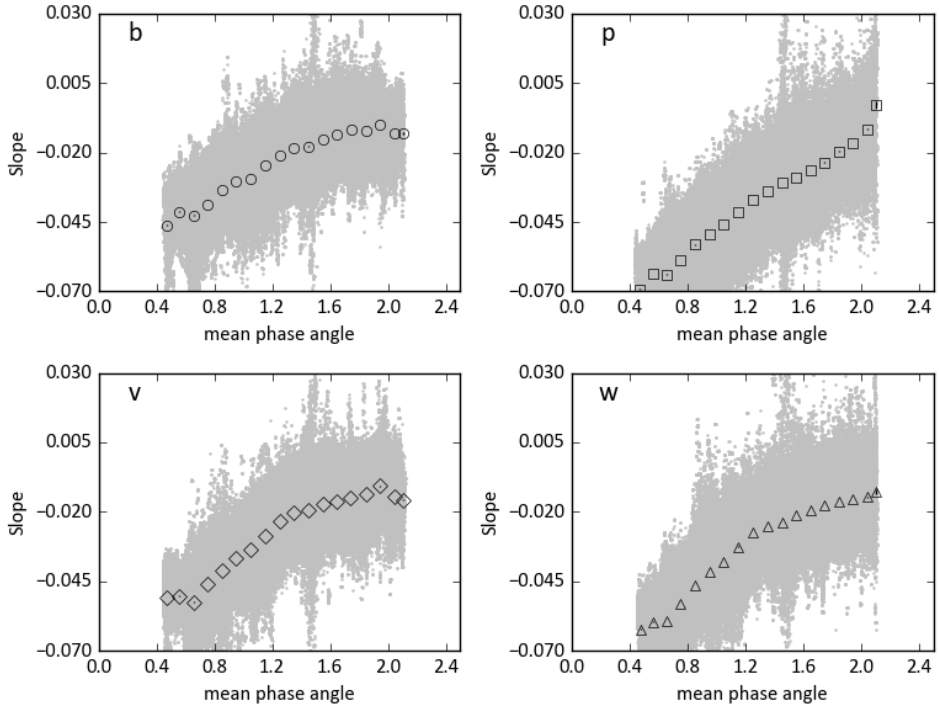

Figure 6 The relationship between phase angle and the slope parameter ($\mathbf{S_{OE}}$) for SET1. The wavelength of AMICA bands is longer in count−clockwise. Gray dots show the original data where the criteria in Section 2.5 are applied. The open symbols mean the averaged $\mathbf{S_{OE}}$ within the bin $\Delta\boldsymbol{\alpha} < \mathbf{0.2}°$. The standard errors of data points are shown here but invisible because it is too small to recognize. This is the plots in case of the incidence angle $i < 90°$.

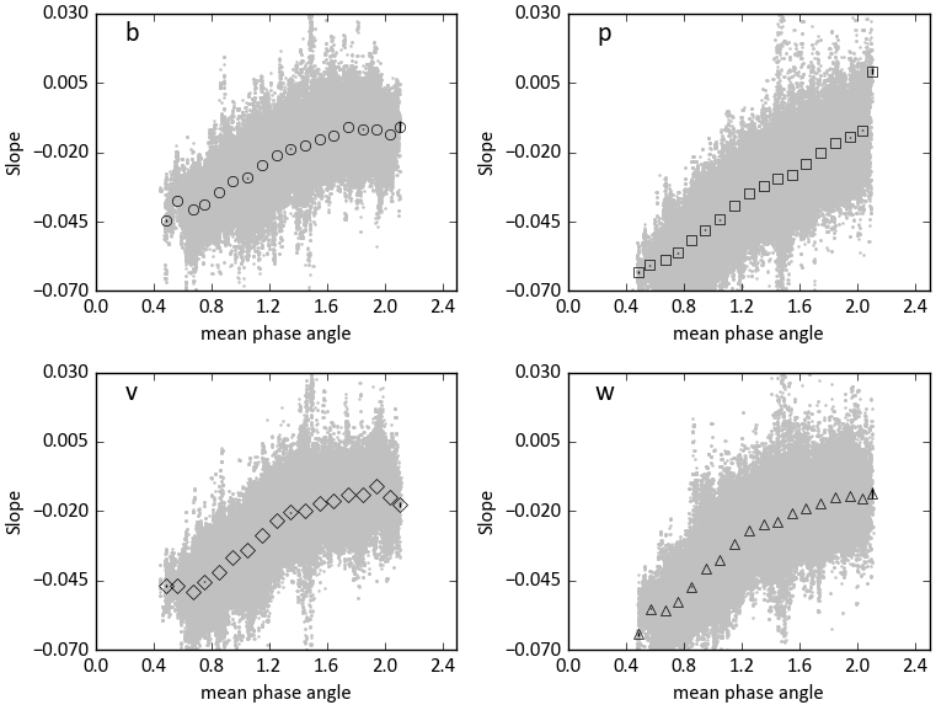

Figure 7 Continued. The same plots with Figure 6. The criterion of the incidence angle is less than 60° is applied.

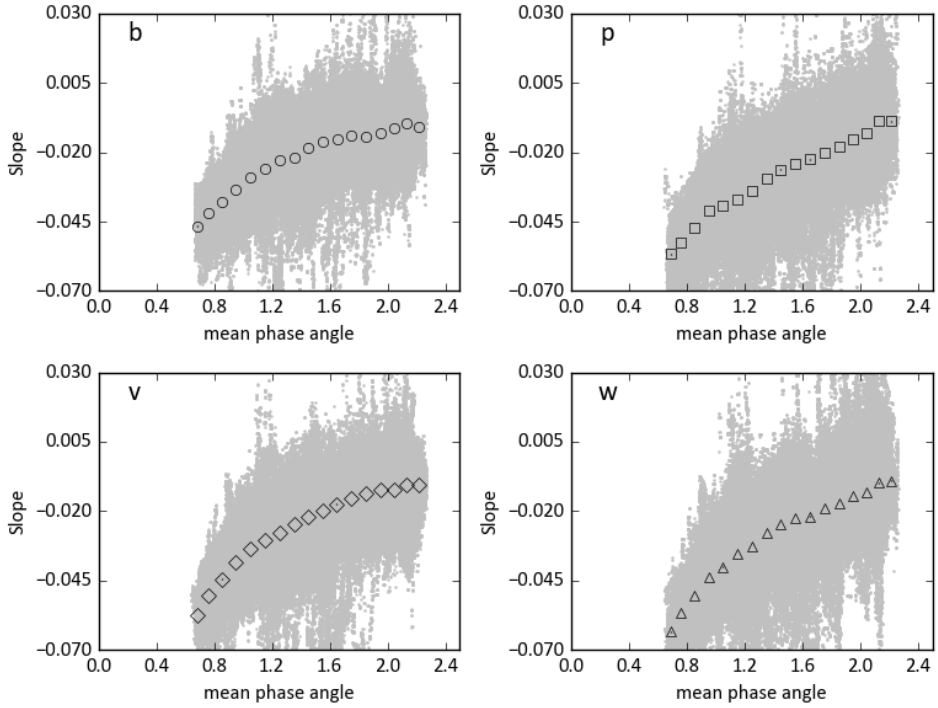

Figure 8 The trend of the relationship between phase angle and the slope parameter ($\mathbf{S_{OE}}$) for SET2. The meaning of dots and symbols are same with those of Figure 6 – Figure 7. The incidence angle is under 90°.

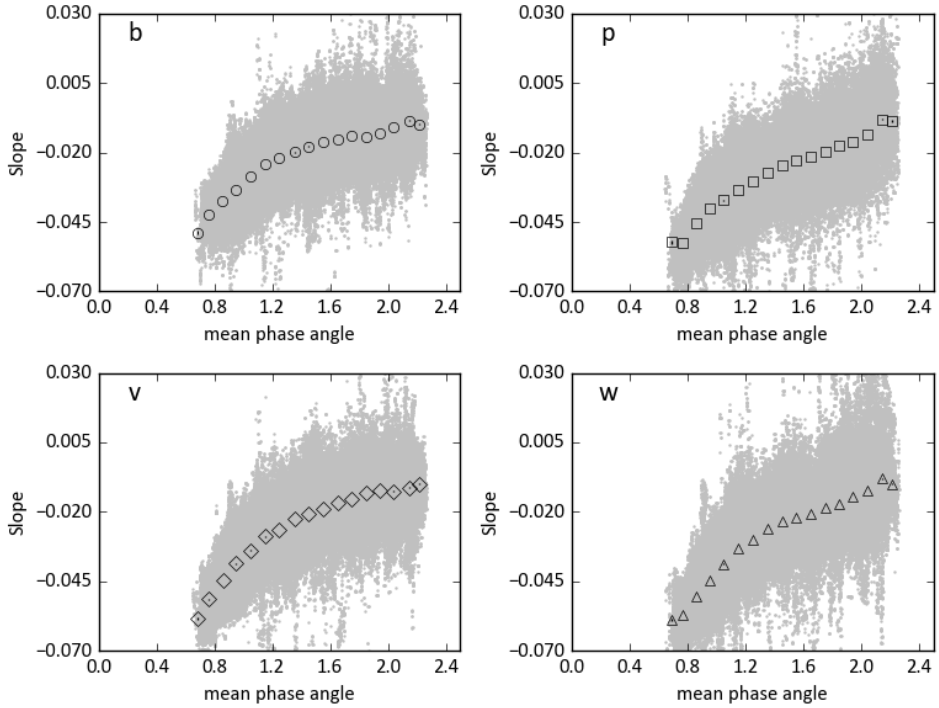

Figure 9 Continued. The incidence angle is less than 60°.

Chapter 4. Interpretation of the Opposition Effect

4.1 The Geometric Angle Dependency of the Opposition Effect on Itokawa

We conducted the study of opposition effect on asteroid Itokawa. A straightforward method was selected for this study rather than the theoretical model as we mentioned in Chapter 2. However, we tried to investigate the influence of the geometric angle with a little help from the theoretical model such as Hapke model to compare with our result. Lederer et al. (2008) analyzed the physical properties of Itokawa with ground-based observation using the integrated form of Hapke model (Hapke 1984). Lederer et al. (2008) could not find certain parameter about opposition effect due to the lack of observation data at smaller phase angles. We fitted Hapke model to the median values of AMICA data in each phase angle 0.5°. For the fitting, we only updated the parameter that corresponds to opposition effect as the free parameter. We followed an integrated form of Hapke model and all other parameters in Lederer et al. (2008). Moreover, the fitting range was limited within the phase angle of 5°. Figure 10 shows the normalized *I/F* as the function of incidence angle derived by Hapke model. More strictly, azimuth angle should be considered to determine phase angle. However, we regarded the azimuth angle as zero, so the phase angle is simplified as $\alpha = i - e$. That is, the incidence angle at horizontal axis in Figure 10 could be treated as the emission angle following condition of opposition, zero phase angle.

We found that the radiance factor *I/F* changes only by less than 3 − 4% of the signal until i=90°. From the result in Chapter 3, the geometric angle, especially incidence (or emission) angle does not affect strength and trend of opposition effect of Itokawa. The good example is the opposition behavior around Yoshinodai boulder:

it is clearly seen in the image at large phase angles while unclear because the large high incidence angle and emission angle around the boulder would not change the radiance factor around the opposition. If these aspects are compelling to the opposition effect, Yoshinodai should have been recognized in S_{OE} map. However, Yoshinodai is invisible in both S_{OE} map and original AMICA image (Red dashed circle in Figure 2). It could demonstrate the validity of our assumption that incidence and emission angles are ineffective to opposition effect of Itokawa.

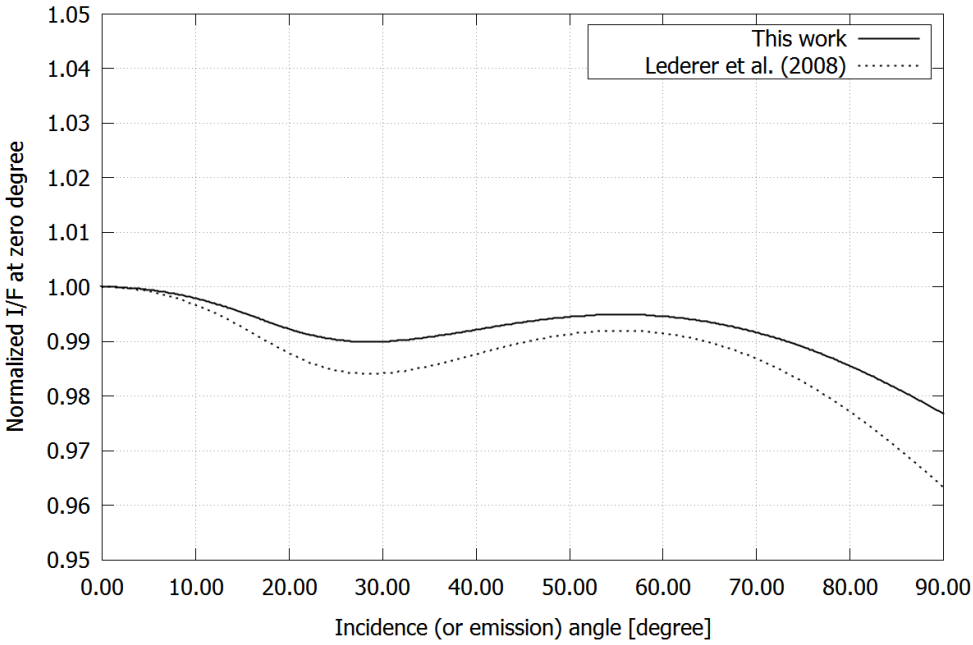

Figure 10 Normalized *I/F* at zero phase angle derived with Hapke model (Hapke 1984). The solid line is the model that opposition parameters are re-derived with AMICA data, while the dashed line is drawn with the parameters in Lederer et al. (2008).

4.2 The Opposition Effect Mechanism

We conducted further analysis about S_{OE} relation with the radiance factor that regarded as albedo. Geometric albedo is an albedo which is defined by the ratio of the integrated brightness on all surface points at opposition to that of the perfect diffusive surface (i.e., the Lambertian surface) with the same area in the same distance. It is a kind of averaged the normal albedo, which is the radiance factor at zero phase angle. The albedo has used for the relationship with opposition effect. It is considered that asteroids that have moderate albedo occur coherent backscattering and shadow-hiding opposition effect simultaneously (Belskaya & Shevchenko 2000; Shkuratov & Helfenstein 2001). Itokawa has the moderate geometric albedo, which is 0.19 (Lederer et al. 2008), or 0.23 by the derivation in our study using AMICA image. We thus may not ignore one of the opposition effect mechanisms for our analysis. Therefore, we investigated S_{OE} with the radiance factor dependency to interpret the dominance of the opposition effect of Itokawa.

We followed similar manner for S_{OE} map illustrated in Figure 5. In Section 3.2, we found that the trend of opposition effect has an inflection point at the phase angle between 1.2 and 1.5°. Centering on the phase angle of 1.4°, we selected three circles that have three different order of albedo but same α_1. To be specific, we specified the circle where both α_1 and α_2 are less than 1.4° (Domain Ⅰ) or greater than 1.4° (Domain Ⅱ). These circles split again into six small sub-regions due to confirmation of regional variation. Once the location of the circles is determined, images of *I/F* and phase angle are aligned with the position to produce manual S_{OE} relation. The *I/F* − S_{OE} relation is illustrated in Figure 11 − Figure 12, and the correlation factor of these two components is shown in Table 3 by using Pearson correlation formula with bootstrapping (Feigelson & Babu 2012).

In Domain Ⅰ, the phase angle is located in the following ranges: $0.58° \leq \alpha <$

1.4° for SET1, and $0.5° \leq \alpha < 1.4$ for SET2. The two sub-panels on the top of Figure 11 − Figure 12, show the clear correlation between *I/F* and S_{OE}. However, the relation for SET1 is more unclear than that of SET2 with the larger standard deviation (error bar on each data point), which seems that it is caused by large variation in remaining the unmatched part. The p-band in SET1 shows small *I/F* change, so it affects the correlation between *I/F* and S_{OE}. However, in SET2, the much stable relation could be seen in Figure 11 − Figure 12 with small standard deviation. For Domain Ⅰ, all data points have S_{OE} values under -0.03, and mostly S_{OE} becomes stronger as *I/F* increase.

Hapke (2002) argued that only coherent-backscattering opposition effect is acted by multiple scattering so that it is proportional to the albedo (and *I/F* as well). Regarding *I/F* at the opposition as the albedo, the strength of the opposition effect has the positive correlation with albedo—for our study, it shows the negative correlation due to the negative sign of S_{OE}—when the coherent backscattering opposition effect occurs. Not only these facts have studied by several authors (e.g. Belskaya & Shevchenko 2000; Hasegawa et al. 2014), but it also corresponds with our study. Combining these elucidations, we conjectured that Itokawa's opposition effect is favorably dominated by coherent backscattering opposition effect under phase angle of 1.4°.

In contrast, this relation in Domain Ⅱ (See second row in Figure 11 − Figure 12) shows no strong correlation between two quantities. The phase angle of selected tiny circles is in the range of $1.54° \leq \alpha < 2.5$, and $1.58° \leq \alpha < 2.5°$ for SET1 and SET2 respectively. All S_{OE} values for Domain Ⅱ has located around -0.01, aligning a straight line no matter what wavelength is. In Table 3, the correlation coefficients do not exceed 0.4. Therefore, *I/F* and the strength of the opposition effect are almost independent each other. As we elucidated in Chapter 1, shadow-hiding opposition

effect is only related with single scattering. From the moderate S_{OE} values and weak *I/F* dependency, it could be suggested that SHOE occupies on Itokawa's surface over the phase angle of 1.4°.

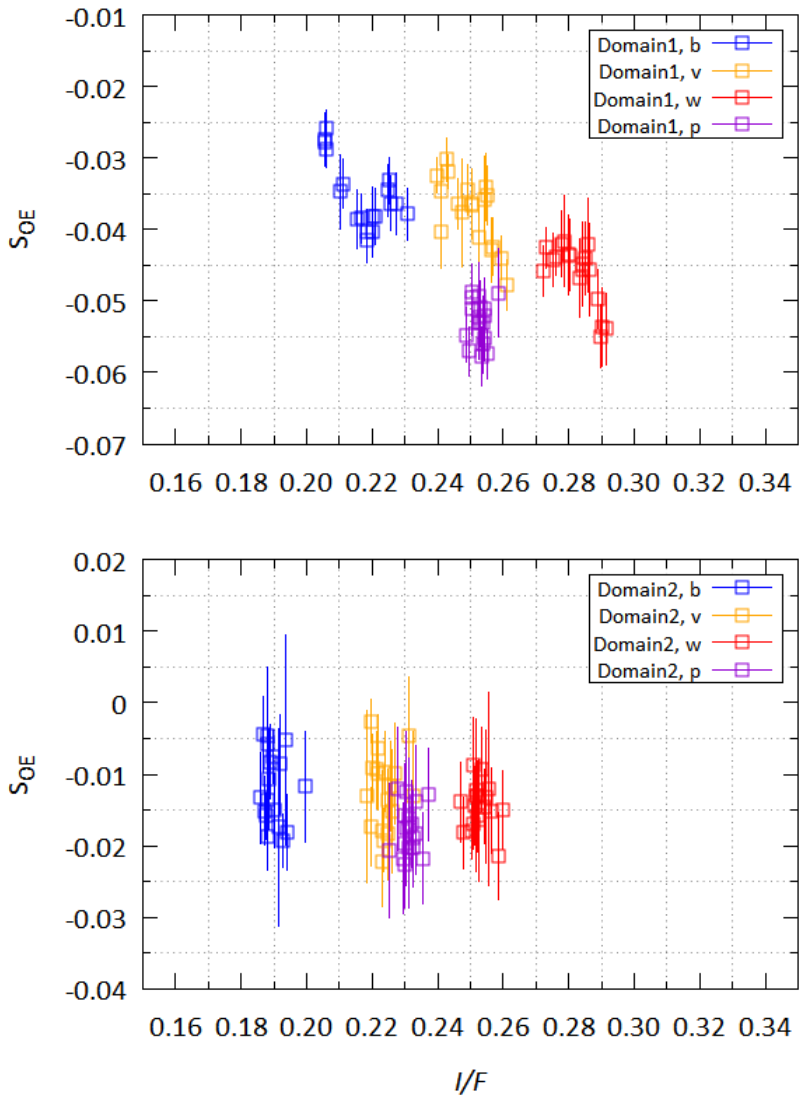

Figure 11 The relationship between mean *I/F* and mean $\mathbf{S_{OE}}$ in Domain I (upper panel) and Domain II (bottom panel) for SET1. Error bars show the standard deviation of sampled regions.

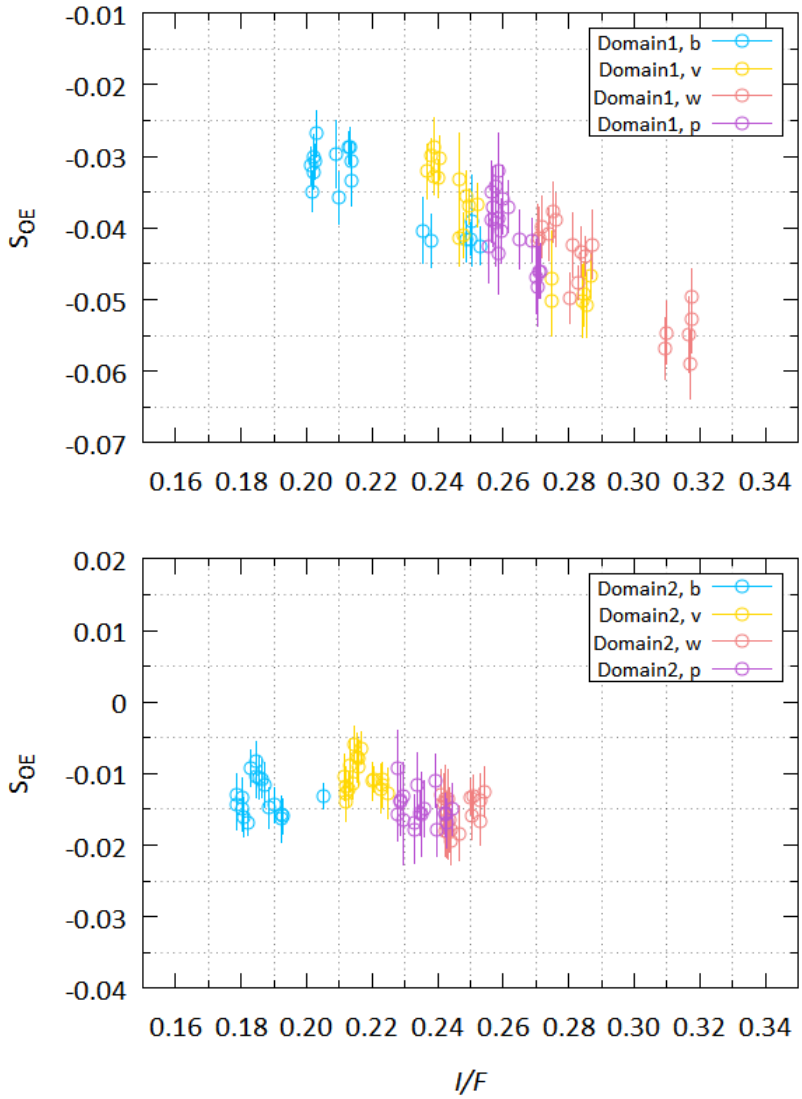

Figure 12 The relation between mean *I/F* and mean S_{OE} in Domain I (upper panel) and Domain II (bottom panel) for SET2. Error bars show the standard deviation of each selected circle

Table 3 The correlation factor between *I/F* and the slope parameter ($\mathbf{S_{OE}}$) illustrated in Figure 11 and Figure 12 with the bootstrap errors (given in the parentheses). The negative sign is due to the relation between phase angle and *I/F*.

	SET1		SET2	
Band	$\alpha < 1.4°$ Domain I	$\alpha > 1.4°$ Domain II	$\alpha < 1.4°$ Domain I	$\alpha > 1.4°$ Domain II
b	−0.66 (0.19)	−0.14 (0.25)	−0.87 (0.12)	−0.11 (0.25)
v	−0.68 (0.18)	0.03 (0.25)	−0.94 (0.008)	−0.12 (0.25)
w	−0.71 (0.25)	−0.13 (0.27)	−0.88 (0.12)	0.33 (0.24)
p	−0.04 (0.25)	0.15 (0.25)	−0.74 (0.17)	−0.3 (0.24)
all	−0.57 (0.1)	0.27 (0.06)	−0.86 (0.06)	−0.33 (0.11)

Chapter 5. Summary

We examined the opposition effect on asteroid Itokawa using eight AMICA images taken in four bands. Specifying a parameter, we investigated the phase angle, the radiance factor (or albedo) and geometric angle (incidence and emission angle) dependencies of the strength of the opposition effect.

With the simple parameter taking account of a linear slope, we found that (1) the opposition effect of Itokawa could be discriminated into two sections separated around $\alpha = 1.4°$, (2) there is no remarkable regional variation on the opposition effect, (3) the incidence and emission angles have little effect on the degree of the opposition effect of Itokawa, (4) there is no significant wavelength dependency for S_{OE}.

We would like to emphasize that we detected the unambiguous evidence for the coherent-backscattering opposition effect on Itokawa under the phase angle of 1.4° while the $I/F - S_{OE}$ relation represents shadow-hiding opposition effect over 1.4°. This discovery may expand the understanding of the opposition effect of small bodies.

References

Belskaya, I. N., Barucci, A. M., & Shkuratov, Y. G. 2003, Earth, Moon Planets, 92 (Kluwer Academic Publishers), 201

Belskaya, I. N., & Shevchenko, V. G. 2000, Icarus, 147, 94

Binzel, R. P., Rivkin, A. S., Bus, S. J., Sunshine, J. M., & Burbine, T. H. 2001, Meteorit Planet Sci, 36, 1167

Buratti, B. J., Hillier, J. K., & Wang, M. 1996, Int J Sol Syst Stud, 124, 490

Déau, E., Dones, L., Rodriguez, S., Charnoz, S., & Brahic, A. 2009, Planet Space Sci, 57, 1282

Demura, H., Kobayashi, S., Nemoto, E., et al. 2006, Science, 312 (American Association for the Advancement of Science), 1347

Dovgopol, A. N., Krugly, Y. N., & Shevchenko, V. G. 1992, ACTA Astron, 42, 67

Feigelson, E. D., & Babu, G. J. 2012, Modern Statistical Methods for Astronomy (Cambridge: Cambridge University Press)

Gehrels, T. 1956, Astrophys J, 123, 331

Gehrels, T., & Taylor, R. C. 1977, Astron J, 82, 229

Hapke, B. 1981, J Geophys Res, 86, 3039

Hapke, B. 1984, Icarus, 59, 41

Hapke, B. 1986, Icarus, 67, 264

Hapke, B. 1990, Icarus, 88, 407

Hapke, B. 2002, Icarus, 157, 523

Hapke, B. 2008, Icarus, 195, 918

Hapke, B. 2012a, Theory of Reflectance and Emittance Spectroscopy (2nd ed.; Cambridge: Cambridge University Press)

Hapke, B. 2012b, Icarus, 221, 1079

Hapke, B. W., Nelson, R. M., & Smythe, W. D. 1993, Science, 260, 509

Harris, A., Young, J. W., Contreiras, L., et al. 1989, Icarus, 81 (Academic Press), 365

Hasegawa, S., Miyasaka, S., Tokimasa, N., et al. 2014, Publ Astron Soc Japan, 66, 89

Hasselmann, P. H., Barucci, M. A., Fornasier, S., et al. 2016, Icarus, 267, 135

Helfenstein, P., Currier, N., Clark, B. E., et al. 1998, Icarus, 135, 41

Helfenstein, P., Veverka, J., & Hillier, J. 1997, Icarus, 128, 2

Ishiguro, M. 2014, Publ Astron Soc Japan, 66 (Oxford University Press), 55

Ishiguro, M., Kuroda, D., Hasegawa, S., et al. 2014, Astrophys J, 792, 74

Ishiguro, M., Nakamura, R., Tholen, D. J., et al. 2010, Icarus, 207, 714

Lederer, S. M., Domingue, D. L., Thomas-Osip, J. E., et al. 2008, Earth, Planets Sp, 60 (Springer Berlin Heidelberg), 49

Lowry, S. C., Weissman, P. R., Hicks, M. D., Whiteley, R. J., & Larson, S. 2005, Icarus, 176, 408

Schaefer, B. E., Rabinowitz, D. L., & Tourtellotte, S. W. 2009, Astron J, 137 (IOP Publishing), 129

Shkuratov, Y. G., & Helfenstein, P. 2001, Icarus, 152, 96

Spjuth, S., Jorda, L., Lamy, P. L., Keller, H. U., & Li, J.-Y. 2012, Icarus, 221, 1101

Verbiscer, A. J., French, R. G., & McGhee, C. A. 2005, Icarus, 173, 66

초 록

태양계 천체 표면에서 반사되는 빛은 위상각(태양–천체–관측자 사이의 각도)이 0도 근처일 때 급격하게 상승하며, 이를 충 효과(opposition effect)라고 한다. 소행성과 카이퍼 벨트 천체 같은 태양계 외곽 소천체들은 주로 위상각 0도 일 때 관측되어왔기 때문에 충 효과는 이 현상이 일어나는 원인을 연구하는 데에 중요한 역할을 한다. 그러나 아직 이 현상의 메커니즘은 아직 많이 연구되지 않았으며, 표면을 구성하는 입자의 그림자가 0도 근처의 위상각에서 가려져 생기는 경우 (shadow hiding opposition effect, SHOE)와, 여러 입자로부터 다중 산란한 빛이 간섭을 일으켜 밝기를 증가시키는 경우 (coherent-backscattering opposition effect, CBOE), 이 두 개가 이론적인 연구를 바탕으로 제시되고 있을 뿐이다. (예: Hapke 1986, 2002)

2005년, 일본의 하야부사(Hayabusa) 미션은 S형 소행성인 (25143) 이토카와(Itokawa)의 표토 샘플 채취에 성공한 바가 있다. 이 미션에서 얻은 이토카와 이미지의 일부는 충 위치일 때 관측된 것으로, 충 효과의 메커니즘에 대한 이해를 도울 수 있는 단서를 제공해 줄 수 있다. 본 연구에서는 소행성 다 파장 이미징 카메라 (Asteroid Multi-band Imaging Camera, AMICA)로 얻은 데이터로, b (429 nm), v (553 nm), w (700 nm), and p (960 nm) 필터에서의 충 효과를, 반사도의 변화량(S_{OE})을 이용하여 분석하였다.

본 연구를 통해 얻은 결과는 다음과 같다. 첫째로, 1.2도 – 1.5도 사이의 위상각에서 S_{OE}는 확실한 변화를 보였지만 그 외의 위상각에서는 거의 일정한 값을 보였다. 두 번째로, 이러한 경향은 네 개의 필터에

대하여 파장에 대한 의존성을 보이지 않았다. 마지막으로, 입사각과 반사각은 S_{OE}에 큰 영향을 미치지 않았다. 이러한 결과들을 토대로 본 연구에서는 1.2도–1.5도 이하의 위상각에선 CBOE가, 그 이상의 위상각에선 SHOE가 충 효과의 주요 메커니즘으로 작용한다는 것을 보였다.

특히, CBOE는 위상각이 매우 작을 때(1.4도 미만), 관측자에 의해 드리워지는 그림자로 인해 태양계 천체에서 그 존재를 직접 확인하기 어렵다. 이런 이유로 본 연구에서는 표면으로부터 멀리 떨어진 거리(약 9km)에서의 관측과 AMICA의 다파장 이미지로 충 효과의 명확한 증거를 찾아낸 것에 의의를 두고자 한다.

주요어: 소행성 – 소행성: (25143) 이토카와 – 소행성: 표면 특성

학 번: 2014-22384